

PAPER • OPEN ACCESS

Terahertz radiative coupling and damping in multilayer graphene

To cite this article: P Bowlan *et al* 2014 *New J. Phys.* **16** 013027

View the [article online](#) for updates and enhancements.

Related content

- [Ultrafast two-dimensional terahertz spectroscopy of elementary excitations in solids](#)
- [Nonperturbative model of harmonic generation in undoped graphene in the terahertz regime](#)
- [Time-resolved spectroscopy on epitaxial graphene in the infrared spectral range: relaxation dynamics and saturation behavior](#)

Recent citations

- [Optimized nonlinear terahertz response of graphene in a parallel-plate waveguide](#)
Parvin Navaeipour and Marc M. Dignam
- [Third-harmonic terahertz generation from graphene in a parallel-plate waveguide](#)
Parvin Navaeipour *et al*
- [Michael Woerner *et al*](#)

Terahertz radiative coupling and damping in multilayer graphene

P Bowlan, E Martinez-Moreno, K Reimann¹, M Woerner and T Elsaesser

Max-Born-Institut für Nichtlineare Optik und Kurzzeitspektroskopie, D-12489 Berlin, Germany
E-mail: reimann@mbi-berlin.de

Received 17 October 2013, revised 10 December 2013

Accepted for publication 17 December 2013

Published 17 January 2014

New Journal of Physics **16** (2014) 013027

[doi:10.1088/1367-2630/16/1/013027](https://doi.org/10.1088/1367-2630/16/1/013027)

Abstract

The nonlinear interaction between intense terahertz (THz) pulses and epitaxial multilayer graphene is studied by field-resolved THz pump–probe spectroscopy. THz excitation results in a transient induced absorption with decay times of a few picoseconds, much faster than carrier recombination in single graphene layers. The decay times increase with decreasing temperature and increasing amplitude of the excitation. This behaviour originates from the predominant coupling of electrons to the electromagnetic field via the very strong interband dipole moment while scattering processes with phonons and impurities play a minor role. The nonlinear response at field amplitudes above 1 kV cm^{-1} is in the carrier-wave Rabi flopping regime with a pronounced coupling of the graphene layers via the radiation field. Theoretical calculations account for the experimental results.

1. Introduction

The electronic band structure of graphene is characterized by double cones in the vicinity of the K and K' points (Dirac points) of the Brillouin zone. The energy increases for the upper or conduction band or decreases for the lower or valence band linearly with the distance from the nearest Dirac point. Accordingly, the electron velocity is independent of the energy and equal to the Fermi velocity [1] $v_F = 10^6 \text{ m s}^{-1}$. Another consequence of graphene's band structure is the

¹ Author to whom any correspondence should be addressed.



Content from this work may be used under the terms of the [Creative Commons Attribution 3.0 licence](https://creativecommons.org/licenses/by/3.0/).

Any further distribution of this work must maintain attribution to the author(s) and the title of the work, journal citation and DOI.

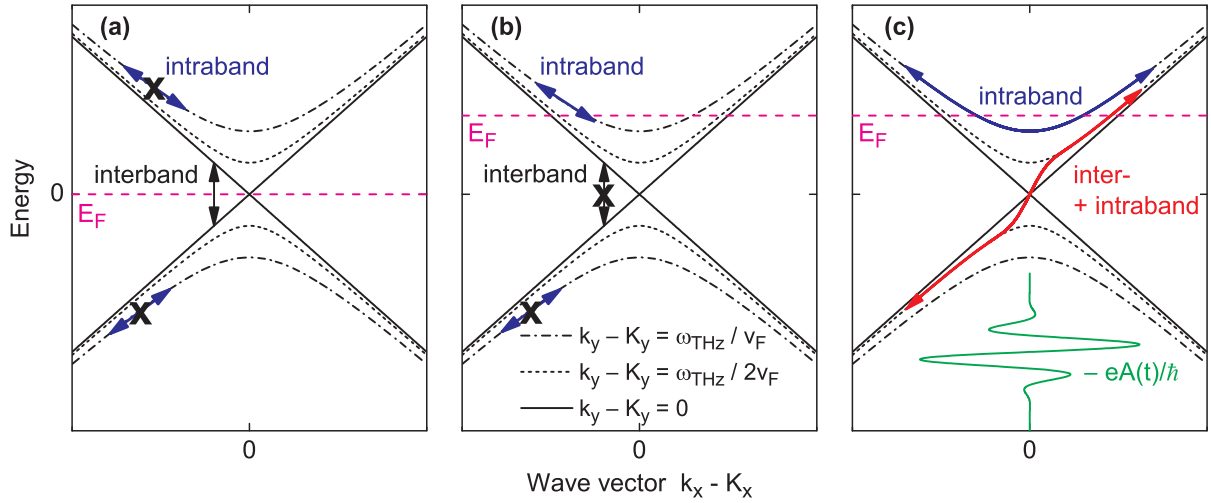


Figure 1. (a) In graphene with $E_F = 0$ at zero temperature interband transitions with arbitrarily low photon energies are allowed, while intraband transitions are not possible. (b) For a finite E_F (shown is the case $E_F > 0$) interband transitions are blocked up to photon energies of $\hbar\omega = 2|E_F|$. On the other hand, electrons in the upper band and holes in the lower band (present for $E_F < 0$) allow for intraband transitions. (c) For high THz field amplitudes the range in k space covered by the intraband trajectories is large enough that the blocking of interband transitions by a finite E_F becomes unimportant. If an electron on such a trajectory reaches a region in k space where the THz field is in resonance with the interband transition frequency, combined inter- and intraband trajectories will occur (lower arrow).

constant optical absorption over a large frequency range, having a value of $\pi\alpha = 0.023$ per layer (α : fine structure constant) [2, 3]. The constant absorption is a result of the cancellation of two effects, a density of states proportional to and a transition dipole moment inversely proportional to the transition frequency. In the terahertz (THz) range this results in a huge interband transition dipole moment, at 2 THz $d = e \times 80$ nm (e : elementary charge).

Because of the huge interband transition dipole moment, one enters the regime of extreme nonlinear optics [4] or the nonperturbative regime in the interaction of electrons with the THz field already for moderate electric field amplitudes. One indication for this behaviour is the interband Rabi frequency $\Omega = dE/\hbar$, which is equal to the THz carrier frequency at a THz field amplitude of 1 kV cm^{-1} . As a consequence strong radiative coupling should occur in multilayer graphene samples where the layer separation is much smaller than the THz wavelength. So far, radiative coupling in multilayer graphene has remained mainly unexplored.

Ideal graphene has a Fermi energy $E_F = 0$, i.e. at zero temperature the lower band is completely filled and the upper band is completely empty. In this case THz absorption is connected with interband transitions, bringing electrons from the valence into the conduction band (figure 1(a)). For a nonzero Fermi energy, interband transitions are blocked up to photon energies $\hbar\omega = 2|E_F|$. On the other hand, electrons in the conduction band (figure 1(b)) (or holes in the valence band) give rise to intraband transitions. Therefore, it is not *a priori* clear whether a finite Fermi energy will result in an increase or a decrease of the absorption in the THz range. The same problem arises when free carriers are generated by optical excitation. There have been several reports on the change of THz absorption after excitation in the near-infrared (NIR) [5–7], in the mid-infrared (MIR) [8], and in the THz range [9–11]. While measurements performed on

single-layer graphene [6, 7, 10, 11] with Fermi energies between -170 and -300 meV show an absorption decrease, measurements on epitaxial multilayer graphene [5, 8, 9] (Fermi energies around 25 meV) show an increase of absorption after excitation.

In this paper, we address the nonlinear THz response of multilayer graphene in pump–probe experiments with a field resolved detection of the pulses. We demonstrate an enhanced transient THz absorption after excitation by ultrashort pulses in the THz, the MIR and the NIR spectral range. The decay of enhanced absorption occurs on a time scale of a few picoseconds. We show that this decay is governed by the predominant interaction with the external THz field, i.e. by radiative coupling and damping. Theoretical calculations account quantitatively for this behaviour.

2. Experiment

The experiments are based on collinear two-dimensional (2D) THz spectroscopy, a technique introduced recently [12, 13]. In the following, we present pump–probe results in the time domain measured in the following way. The output from a femtosecond Ti:sapphire oscillator–amplifier system is split and sent into two GaSe crystals to generate two phase-locked THz pulses A and B by optical rectification [14]. The two pulses with a spectral maximum at 2 THz and a mutual delay τ interact with the graphene sample. The transmitted electric-field transients are measured by electro-optic sampling [15] in a ZnTe crystal. Two choppers synchronized to the pulse repetition rate allow for measuring the electric-field transients $E_{AB}(t, \tau)$ (both pulses A and B are incident on the sample), $E_A(t)$ (only pulse A) and $E_B(t, \tau)$ (only pulse B). The nonlinear signal emitted from the sample, which is proportional to the nonlinear current in the sample [16], is the difference

$$E_{NL}(t, \tau) = E_{AB}(t, \tau) - E_A(t) - E_B(t, \tau) \quad (1)$$

and depends on the delay τ and the real time t .

The graphene samples grown by C-face epitaxy on SiC (from Graphene Works) contain 45 layers. Electronic coupling between the layers is negligible [17]. The spectrally integrated linear transmission of the sample at $T = 300$ K was 0.36, as measured with THz pulses of a low electric field amplitude of 0.2 kV cm^{-1} . A detailed analysis shows that the linear THz transmission spectra are dominated by intraband (Drude) absorption with an average Fermi energy of $E_F = 24$ meV and a Drude scattering time of $T_s = 40$ fs.

3. Experimental results

Time-resolved THz transients measured with excitation pulses in the THz, MIR and NIR spectral range are summarized in figure 2. The electric field of the THz probe pulse and the nonlinear signal E_{NL} are plotted as a function of real time t , the pump–probe delay was $\tau = 0$. Independent of the pump wavelength the nonlinear signal displays a phase opposite to the driving electric field, indicating induced absorption.

In the following we concentrate on the dependence of the induced absorption on the delay τ between the two THz pulses. To extract from our 2D data the customary pump–probe signals, we perform a 2D Fourier transform of the nonlinear signal $E_{NL}(t, \tau)$ and filter out the pump–probe

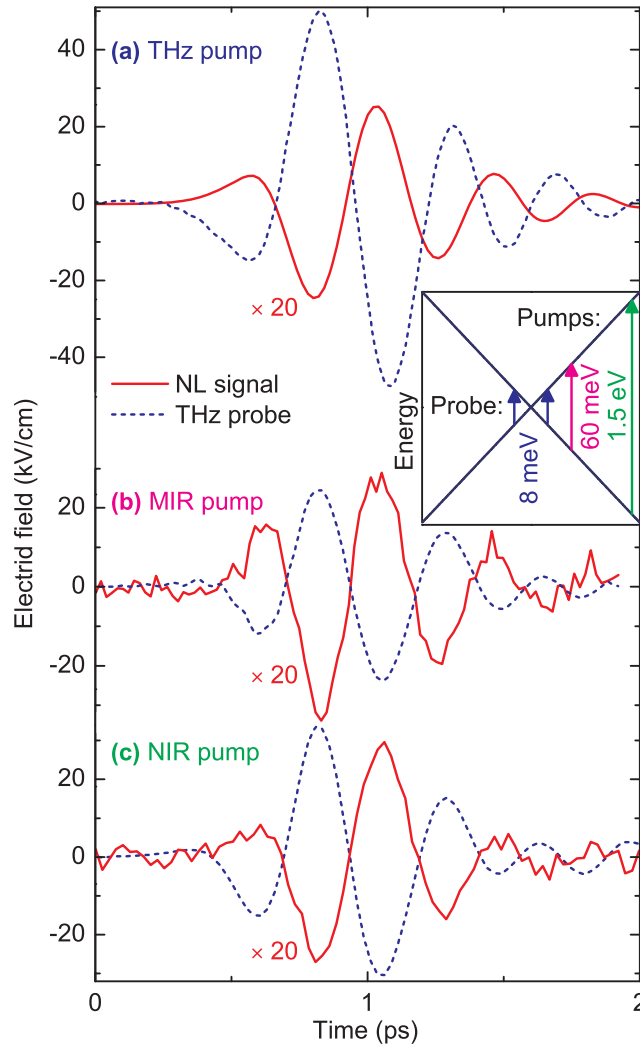


Figure 2. Solid lines: measured pump–THz-probe signals at room temperature at a delay $\tau = 0$ for different pump photon energies, (a) 8 meV, (b) 60 meV and (c) 1.5 eV. Dashed lines: THz probe pulses. The inset shows schematically the pump and probe transitions in graphene’s band structure.

signal in the frequency domain [9, 13]. After a Fourier transform back into the time domain we get the pump–probe signal $E_{PP}(t, \tau)$. With this the differential transmission is given by

$$\frac{\Delta T}{T_0}(\tau) = \frac{2 \int E_{pr}(t, \tau) E_{PP}(t, \tau) dt}{\int E_{pr}^2(t, \tau) dt}. \quad (2)$$

The probe field E_{pr} can be either E_A or E_B , depending on which signal was chosen in the frequency domain. Results for the differential transmission $\Delta T/T_0(\tau)$ obtained from (2) are shown for different sample temperatures in figure 3(a) and for different amplitudes of the THz field in figure 3(b). In all cases the transmission decreases (induced absorption) upon pumping. The transmission recovers with time constants τ_d between 1.8 and 4.5 ps, as obtained from single-exponential fits (dashed lines in figure 3). These times are surprisingly short compared to

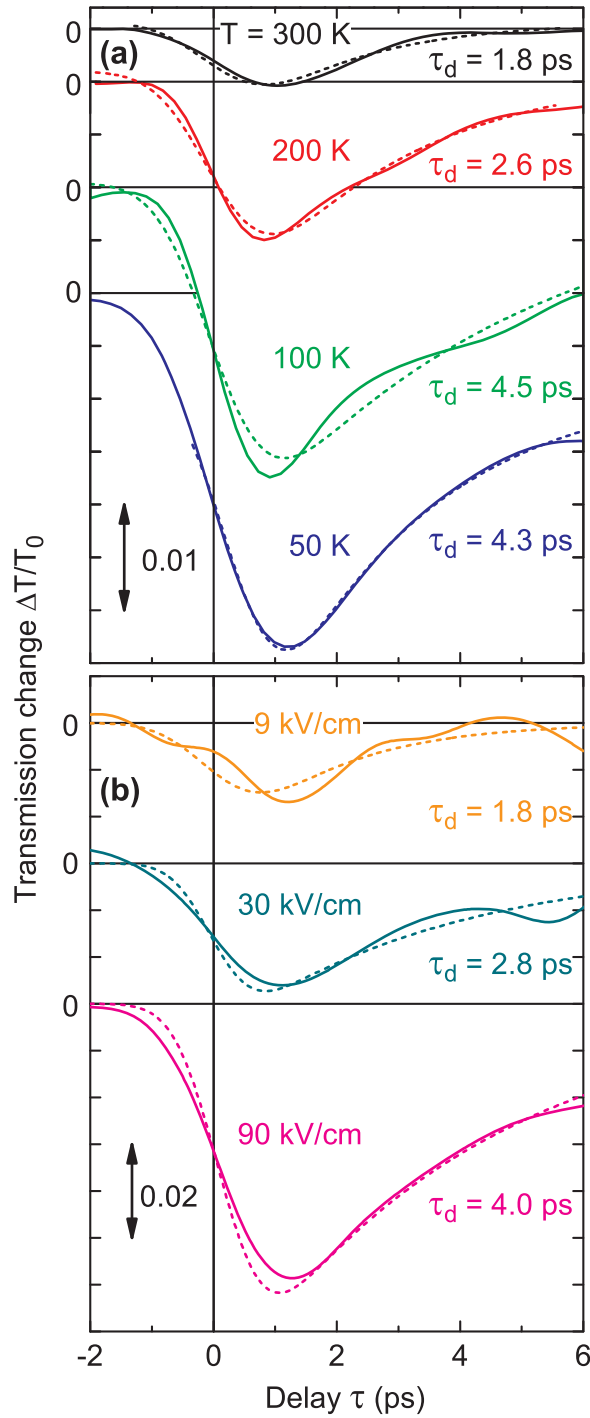


Figure 3. Measured pump-probe signals (a) for different sample temperatures T (THz electric field amplitude 5 kV cm^{-1}) and (b) at room temperature for different electric field amplitudes. Solid lines: experimental results; dashed lines: single-exponential fits with decay times τ_d as indicated.

the experimental data in [5, 8]. The decay times increase with decreasing temperature and with increasing THz field amplitude. The magnitude of the differential transmission increases with decreasing temperature.

4. Discussion

We first present a numerical estimate underlining the importance of radiative coupling in multilayer graphene. Considering only interband transitions in a fully coherent picture and assuming that all polarizations are parallel, the amplitude of the coherent interband current at a point in k space is $e v_F$. Integrating this current over the part of the Brillouin zone with interband transition frequencies between ω_1 and ω_2 yields the total one-dimensional (1D) current density per layer of $J = e(\omega_2^2 - \omega_1^2)/(16\pi v_F)$. This current density corresponds to an emitted field of $E_{\text{em}} = N Z_0 J/(1 + n_{\text{sub}})$ with $N = 45$ the number of layers, $Z_0 = 377 \Omega$ the vacuum impedance and $n_{\text{sub}} = 3.1$ the refractive index of the substrate [18]. The emitted field leads to an energy loss rate of $L = (1 + n_{\text{sub}})E_{\text{em}}^2/Z_0$. On the other hand, the energy content, i.e. $\hbar\omega/2$ integrated over the same part of the Brillouin zone is $W = N\hbar(\omega_2^3 - \omega_1^3)/(48\pi v_F^2)$. Thus, for a fully coherent emission the energy content has a radiative lifetime $T_{\text{rad}} = W/L$. Using the frequency range relevant for our experiment ($\omega_1 = 2\pi \times 1$ THz, $\omega_2 = 2\pi \times 3$ THz), we find $T_{\text{rad}} = 1$ ps. This value is in the same order of magnitude as the observed decay times of induced absorption in figure 3, suggesting a strong influence of radiative coupling on the measured transients.

We now address a key result of our experiments, the observation of induced absorption after THz, MIR and NIR excitation (cf figures 2 and 3). This finding has to be reconciled with the observation of an absorption decrease in samples with $|E_F| > 100$ meV. NIR pump pulses at 1.5 eV excite electrons from the valence into the conduction band for all samples studied so far, since Pauli blocking of optically coupled states is absent even for the highest $|E_F| \approx 300$ meV [5–7]. For samples with $E_F \approx 25$ meV [8], this is also true for MIR excitation. The generated electrons and holes thermalize on a time scale of the order of 100 fs into quasi-Fermi distributions with an elevated carrier temperature [19], a process generating a free carrier population close to the K points. This distribution leads to a *reduced* interband absorption because of Pauli blocking and to an *enhanced* intraband absorption because of enhanced electron and hole densities. The higher carrier temperature, on the other hand, has the opposite effect, namely an *increased* absorption on interband transitions for which Pauli blocking is reduced, and a *reduced* absorption from intraband transitions as—at higher temperature—carriers move into regions of k space where they have larger effective masses². It is not *a priori* clear which of these effects dominates. The difference in the sign of the transient absorption change for different E_F can be explained by considering that intraband transitions are the dominant cause of THz absorption. For samples with large $|E_F|$, i.e. a large density of free carriers, the main effect of pumping is the temperature increase, leading to reduced absorption, whereas in samples with low $|E_F|$ the main effect is the increase in carrier density, leading to increased absorption. Our sample with an average $|E_F| = 24$ meV exhibits the latter behaviour.

Our data display an amplitude of induced absorption that increases with increasing amplitude of the pump field (figure 3(b)) and decreasing lattice temperature (figure 3(a)). With increasing pump field, the free carrier densities in the valence and conduction band and, thus, the intraband absorption strength are enhanced. At low lattice temperature, the initial density of free carriers is small and pumping induces a strong increase in carrier density and differential absorption. At higher lattice temperature, the substantially higher initial free carrier density

² Even in the cone approximation electrons (apart from those exactly at the K and K' points) in graphene have a finite effective mass tensor. While the magnitude of their velocity is constant, its direction can change under the influence of an external force.

and the partial (Pauli) blocking of interband THz excitation of extra carriers result in a smaller differential signal.

Before addressing the picosecond decay times of the nonlinear THz signal, we briefly consider a potential influence of scattering processes on the observed kinetics. The energy range considered here is far below the optical phonon frequency of 45 THz [20] and, consequently, optical phonon emission plays a minor role. For sample temperatures up to 300 K, the thermal optical phonon population is very small, ruling out optical phonon absorption as well. Acoustic phonons have much lower energies, but their coupling to electrons is quite weak, resulting in decay times of a THz driven current on a time scale of 100 ps [21], much longer than the decays we observe. The recently predicted supercollisions [20, 22], i.e. disorder-assisted electron–acoustic-phonon scattering, lead to a strong temperature dependence and to decay times of the same order of magnitude as our results. However, this mechanism leads to a decrease of the decay time τ_d with increasing pump field, in contrast to our observations. If electron–electron scattering would be the dominant scattering process, τ_d should decrease with increasing pump field and carrier density, again in contrast to our experimental results.

To account for the picosecond decays of the THz signals, radiative coupling within the multilayer sample was considered within a model which incorporates the electronic bandstructure and the coupling of carriers to the THz field but neglects scattering processes. To describe radiative coupling, we include not only the action of the electric field on the electrons, but also the influence of the electrons on the electric field. It turns out that this simple model is sufficient to describe all our results. While the cone approximation [23], in which the valence and conduction bands are mirror images of each other, is sufficient to account for the observed induced absorption and for the absence of photon-echo signals [9], it fails in predicting the picosecond decay times. A quantitative treatment of the latter requires an electronic band structure that correctly includes the threefold symmetry around the K points and the differences between upper and lower bands.

To describe the threefold symmetry of the band structure around the K point correctly, one has to consider the hexagonal lattice symmetry of graphene. One possibility to do this is a tight-binding calculation [1, 24], in which the Bloch functions are composed of atomic orbitals centred at the positions of the atoms. In the simplest way just one type of atomic orbital is used, which leads to two bands as the primitive unit cell contains two C atoms. Another possibility is the pseudopotential method [25–27]. The pseudopotential form factors can be obtained either from first-principles calculations or from a fit to experimentally determined energies at certain points in the Brillouin zone (empirical pseudopotential). For our calculations we used such empirical pseudopotential band structure (see the [appendix](#) for more details). The pseudopotential method yields THz transmission values in agreement with the experiment (at low temperatures the THz transmission is determined by the quantum conductivity [2, 3, 28] σ_0). A comparison of the different band structure calculations is shown in figure 4. They agree at the K point and show a difference in carrier energy of less than 0.2 eV up to a tenth of the Brillouin zone around the K point. At larger k vectors, the energy differences are significant.

Since the stack of graphene layers is much thinner than all optical wavelengths involved, the local electric field is the same in all layers. The local electric field consists of the incident electric field $E_{\text{in}}(t)$, of the electric field emitted by the electrons $E_{\text{em}}(t)$ (in this way the radiative coupling is included), and of the electric field reflected at the interface between the substrate and the graphene $E_{\text{sub}}(t)$. In this geometry the local electric field is equal to the transmitted field [16]

$$E_{\text{tr}}(t) = E_{\text{in}}(t) + E_{\text{em}}(t) + E_{\text{sub}}(t). \quad (3)$$

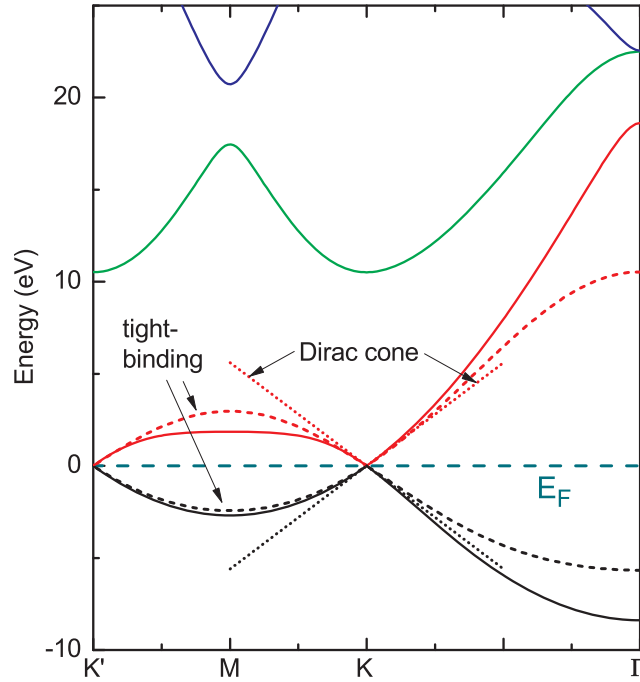


Figure 4. Band structure of graphene. Solid lines: pseudopotential calculation using 21 reciprocal lattice vectors of the 2D crystal. Dashed lines: two-band tight-binding model [1]. Dotted lines: Dirac cone around K . In an undoped graphene sample the Fermi level E_F meets exactly the tips of the two Dirac cones at K and K' .

We use the long-wavelength approximation [29], i.e. neglect the influence of the magnetic field and assume that the electric field in the sample is spatially homogeneous, i.e. only time-dependent. This gives a spatially constant vector potential

$$A(t) = \int_{-\infty}^t E_{\text{tr}}(t') dt'. \quad (4)$$

For a sample consisting of N graphene layers the emitted field is given by [30]

$$E_{\text{em}}(t) = -\frac{N Z_0}{2} J(t). \quad (5)$$

The 2D current density $J(t)$ is the current density of a single graphene layer. If the graphene layers are on a substrate (in our case hexagonal SiC [17]), the refractive index jump at the interface also emits a field

$$E_{\text{sub}}(t) = \frac{1 - n_{\text{sub}}}{2} E_{\text{tr}}(t) \quad (6)$$

determined by the refractive index n_{sub} of the substrate [18]. Both the field emitted by the stack of graphene layers and by the substrate modify the driving vector potential of the system. As a result the influence of $E_{\text{em}}(t)$ on $A(t)$ causes coherent radiative damping of the entire system.

For the linear THz response of graphene, i.e. for low THz fields, the present model based on pseudopotential band-structure calculations gives identical results to those of the widespread conductivity model [2, 5, 28, 31–35]. To account for the finite broadening of intra- and interband transitions and to achieve irreversible absorption, in the linear regime we

introduced a phenomenological friction force. In the nonlinear regime, there is no need for such a phenomenological damping, since losses due to radiative coupling and damping become dominant.

Intraband transitions in the absence of scattering are governed by the acceleration theorem, i.e. $d\vec{k}/dt = -e\vec{E}(t)/\hbar$ (figure 1). A THz pulse polarized in x -direction³ moves an electron back and forth in k space along a trajectory given by $k_x(t) = k_x(0) - eA_x(t)/\hbar$ determined by the transient vector potential $A_x(t)$ (k_y remains constant). For constant k_y the band structure $\mathcal{E}(k_x, k_y = \text{const.} \neq 0)$ as a function of $k_x - K_x$ follows two hyperbolas (valence and conduction band). For an electron residing initially at \vec{k} with $|k_y - K_y| > \omega_{\text{THz}}/2v_F$ resonant interband transitions are not possible so that the intraband current (motion of the carrier along the upper double arrow in figure 1(c)) dominates the response to the applied THz field.

This behaviour changes for electrons residing initially at k vectors with $|k_y - K_y| < \omega_{\text{THz}}/2v_F$. In this case the change in k_x introduced by the electric field brings the electrons to points in k space where the difference between valence and conduction band is resonant to the THz frequency. As a result, they perform trajectories as visualized by the lower double arrow in figure 1(c). Because of the extremely strong transition dipole the light–matter interaction is inherently in the nonperturbative regime and dominates over the interactions underlying scattering processes of the carriers.

The trajectories shown in figure 1 are only possible if the initial state is filled and the final state is empty. Thus, if the valence band is completely filled, the intraband current is zero. The same is true for an empty conduction band. Considering the case of a finite Fermi level E_F at zero temperature, for low field amplitudes interband transitions are not possible if $2|E_F| > \hbar\omega_{\text{THz}}$. However, because the intraband motion happens simultaneously, even with a finite E_F interband transitions become possible provided the field strength is large enough ($e v_F \max(|A(t)|) > |E_F|$). For the field strengths used in our experiment this means that Fermi levels $|E_F| \approx 25$ meV, as obtained from linear absorption measurements, yield essentially the same results as $E_F = 0$.

Our theory provides k -resolved populations and polarizations (figure 5). These results illustrate in detail why the radiative damping is faster when less energy is deposited in the sample, as is the case at higher lattice temperatures. In figure 5(a), the calculated electron distribution $\rho_{22}(k_x, k_y)$ in the upper Dirac cone around K is shown after interaction with a THz pulse polarized along the x -direction with a very small electric field amplitude of 30 V cm^{-1} . For symmetry reasons the distribution functions in the cone around K' are mirror images of those around K . The corresponding carrier distribution $\rho_{22}(k_x, k_y)$ is essentially the product of the spectral density of the THz pulse with the modulus squared of the dipole matrix elements. After interaction with the driving pulse, the electron distribution in the upper cone $\rho_{22}(k_x, k_y)$ has a very short lifetime, since radiative damping in the 40-layer graphene sample is extraordinarily strong. Thus, for very low THz fields the model predicts a decay within the pulse duration.

The situation changes in the nonperturbative regime. In figure 5(b) we plot $\rho_{22}(k_x, k_y)$ after interaction with a THz pulse with an amplitude of 3 kV cm^{-1} . The generated electron distribution $\rho_{22}(k_x, k_y)$ shows a speckle-like structure due to the chaotic phase distribution in k space of the concomitantly generated coherent interband polarizations shown in figure 5(d). The reason for the chaotic phases are the different Rabi frequencies at each point in k space. While for low field amplitude (figures 5(a) and (c)) all electrons in the upper band have the same phase

³ Ishikawa [24] and we (following [1]) use different conventions for the directions, his x is our y and vice versa.

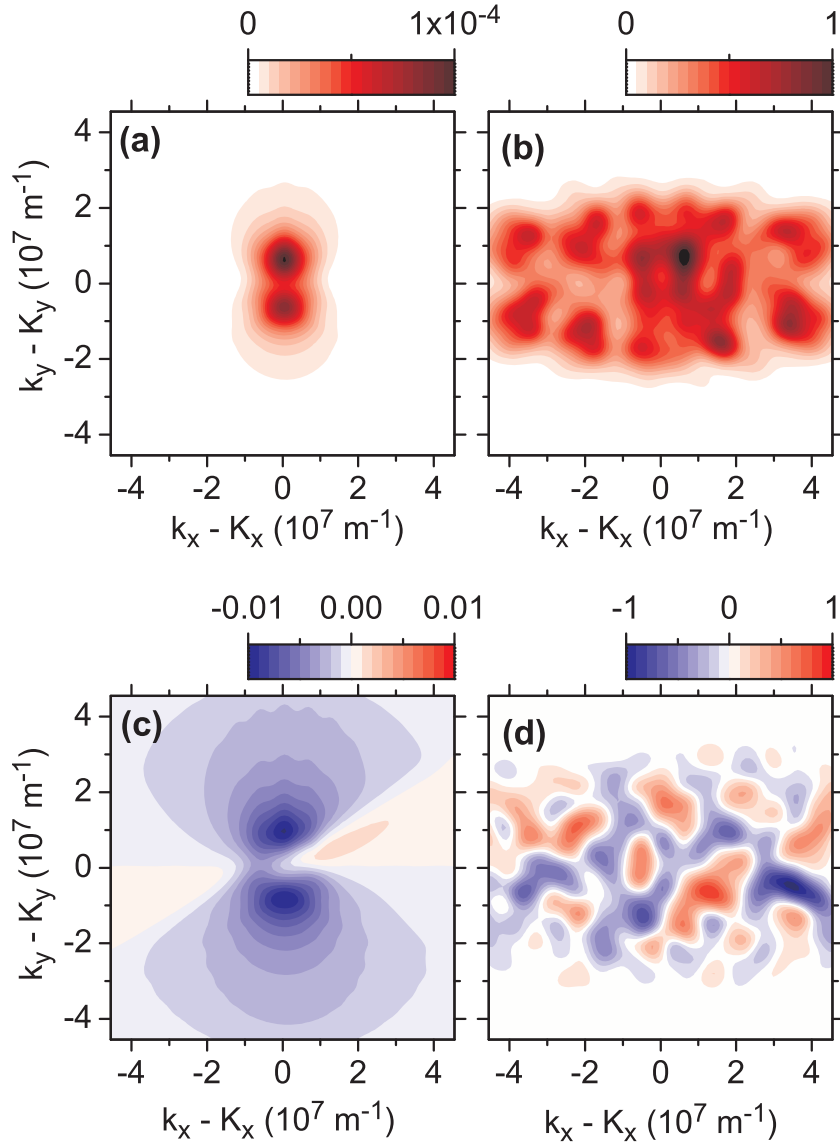


Figure 5. (a), (b) Calculated electron populations in the upper band $\rho_{22}(k_x, k_y)$ around K , (c) and (d) corresponding real part of the off-diagonal density matrix elements $2 \text{Re}[\rho_{12}(k_x, k_y)]$, after interaction with a THz pulse polarized along x with an amplitude of (a) and (c) 30 V cm^{-1} (perturbative regime) and (b) and (d) 3 kV cm^{-1} (nonperturbative regime).

and thus can emit coherently, for high field amplitude (figures 5(b) and (d)) this is only true for the electrons within a speckle. Our theory predicts a radiative damping rate that decreases with the number of speckles within this chaotic ensemble. The number of speckles increases with the stored energy. Since the signal strength is proportional to the stored energy, one expects the behaviour experimentally observed in figures 3(b) and 6. With increasing temperature, the picosecond decay of the enhanced absorption becomes faster and the amplitude of the pump-induced absorption decreases (figure 3(a)). The experimentally observed temperature-dependent damping rate originates from the temperature-dependent initial electron populations.

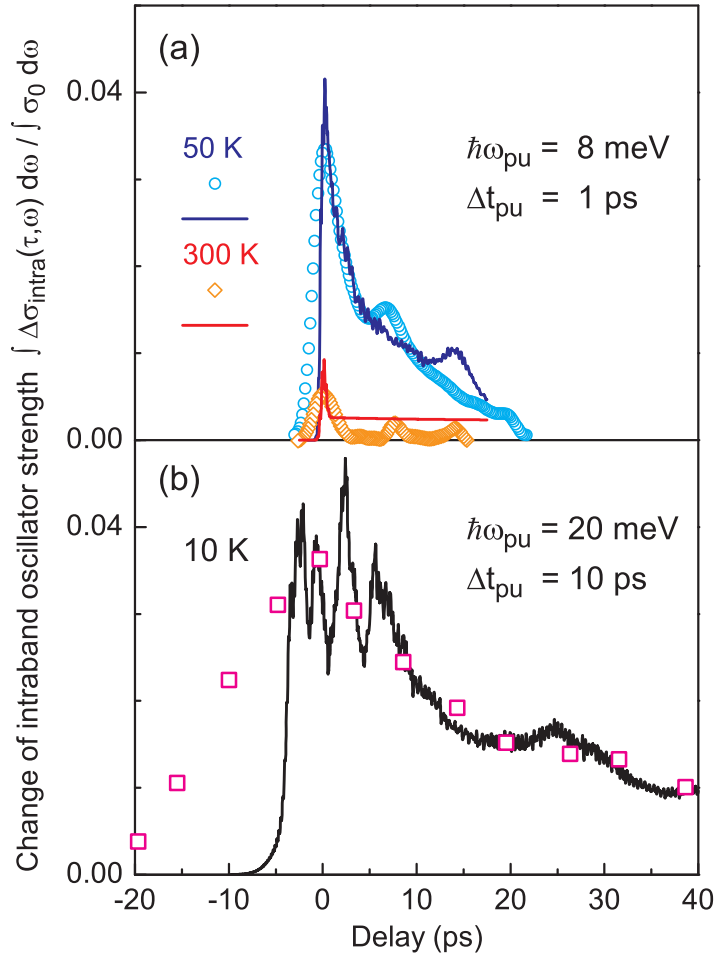


Figure 6. (a), (b) Calculated population recovery due to radiative damping (solid lines) in comparison with various experimental situations (symbols). The transient change of the intraband oscillator strength $\int \Delta\sigma_{\text{intra}}(\tau, \omega) d\omega / \int \sigma_0 d\omega$ is plotted as a function of the delay for different THz pump pulses and lattice temperatures. The open squares in (b) are experimental results from [8].

The sample converts the initial coherent THz radiation at 2 THz into broad-band chaotic radiation (still coherent) with frequencies up to a cutoff frequency given by the highest transition frequency encountered during the intraband trajectory. The new frequency components can in turn be reabsorbed and reemitted via interband transitions that were initially not in resonance with the THz pulse. This multi-frequency character of the overall THz field emitted by the sample explains the absence of photon-echo signals in the nonlinear response [9]. The interband Rabi frequency is different at each point in k space, due to both the \vec{k} -dependent interband dipole moment and the different electric field amplitudes $E(\omega)$ at different interband transition frequencies. Thus, a coherent rephasing of the different contributions by interaction with the THz driving field is impossible and the total photon-echo signal is negligible.

In the nonperturbative regime, the coupling of the carriers to the external THz field is much stronger than the interaction among the carriers and interactions of carriers with the lattice. As a consequence, carrier dynamics are governed by the highly nonlinear interaction with the THz

field rather than by scattering processes. Under such conditions, the single-particle picture of carrier dynamics applied here represents a realistic description of the experimental scenario.

Finally, we compare the picosecond decays of enhanced absorption measured at different lattice temperatures (figure 3(a)) and the experimental results of [8] with the predictions of our theory. For a direct comparison, the transient change of the intraband oscillator strength $\int \Delta\sigma_{\text{intra}}(\tau, \omega) d\omega / \int \sigma_0 d\omega$ was calculated with (4) of [5]. In figure 6, this quantity is plotted as a function of pump–probe delay for different THz pump pulses and lattice temperatures. In panel (a) we compare the calculated change of the intraband oscillator strength for a 1 ps pump pulse at $\hbar\omega = 8$ meV and a field amplitude of $E_{\text{pu}} = 5$ kV cm⁻¹ with our experiments performed at temperatures of 50 and 300 K.⁴ In panel (b) we calculated such a transient for a longer (10 ps) pump pulse at a higher photon energy, $\hbar\omega = 20$ meV, with a field amplitude of $E_{\text{pu}} = 2.4$ kV cm⁻¹, corresponding to the $\Phi = 0.4$ $\mu\text{J cm}^{-2}$ transient from figure 3(b) of [8]. These results show that the decay depends strongly on the energy deposited in the sample. Longer pulses (figure 6(b)) deposit more energy in the sample, leading to longer decays than shorter pulses (figure 6(a)). The good agreement of theory and experiments reveals the prominent role of radiative damping for energy relaxation of the carriers while scattering processes play a minor role under the present conditions.

5. Conclusions

Using collinear 2D THz spectroscopy we have studied the nonlinear dynamics of electrons in multilayer graphene. Instead of the expected bleaching due to the saturation of interband absorption, the pump–probe signals show induced absorption, which decays with time constants of a few picoseconds. The time constants decrease with increasing temperature and increase with increasing energy density deposited. Our results are fully explained by theoretical calculations using a pseudopotential band structure for graphene and including radiative coupling and damping. Under the present conditions of strong radiative coupling in a multilayer sample, fast decoherence processes or other scattering mechanisms play a minor role for the nonequilibrium response to the external THz field.

Acknowledgment

The authors thank the Deutsche Forschungsgemeinschaft for financial support (RE 806/9-1).

Appendix. Pseudopotential band structure

The potential $V(\vec{r})$ in the single-particle Hamiltonian

$$H = \frac{p^2}{2m} + V(\vec{r}) \quad (\text{A.1})$$

has in a crystalline solid the periodicity of the crystal lattice. This allows $V(\vec{r})$ to be written as

$$V(\vec{r}) = \sum_{\vec{G}} V_{\vec{G}} \exp(i\vec{G}\vec{r}). \quad (\text{A.2})$$

⁴ In figure 6(a), the plateau in the theoretical curve for $T = 300$ K at later times is an artefact of including only radiative damping in the calculation. Very weak additional damping would remove this plateau without influencing the decay time.

The sum extends over all reciprocal lattice vectors \vec{G} . The solutions of (A.1) have according to the Bloch theorem [36] the form

$$\psi_{n,\vec{k}}(\vec{r}) = \exp(i\vec{k}\vec{r}) u_{n,\vec{k}}(\vec{r}) \quad (\text{A.3})$$

with $u_{n,\vec{k}}(\vec{r})$ having the periodicity of the lattice. Thus, similar to (A.2), $\psi_{n,\vec{k}}(\vec{r})$ can be written as

$$\psi_{n,\vec{k}}(\vec{r}) = \exp(i\vec{k}\vec{r}) \sum_{\vec{G}} c_{\vec{G}} \exp(i\vec{G}\vec{r}) \quad (\text{A.4})$$

i.e. $\psi_{n,\vec{k}}(\vec{r})$ is uniquely determined by the set of $c_{\vec{G}}$. Inserting (A.2) and (A.4) into (A.1) results in

$$H(\vec{k}) = \begin{pmatrix} \frac{\hbar^2(\vec{k}+\vec{G}_0)^2}{2m} & V_{\vec{G}_1-\vec{G}_0} & V_{\vec{G}_2-\vec{G}_0} & \cdots \\ V_{\vec{G}_0-\vec{G}_1} & \frac{\hbar^2(\vec{k}+\vec{G}_1)^2}{2m} & V_{\vec{G}_2-\vec{G}_1} & \cdots \\ V_{\vec{G}_0-\vec{G}_2} & V_{\vec{G}_1-\vec{G}_2} & \frac{\hbar^2(\vec{k}+\vec{G}_2)^2}{2m} & \cdots \\ \vdots & \vdots & \vdots & \ddots \end{pmatrix}. \quad (\text{A.5})$$

The eigenvalues of $H(\vec{k})$ for all \vec{k} in the first Brillouin zone then yield the electronic band structure.

For every numerical calculation one limits the infinite sum in (A.4) to a finite subset of reciprocal lattice vectors (total number Z), so that $H(\vec{k})$ becomes a $Z \times Z$ matrix. In this case at most Z Fourier components of the potential can contribute.

Since graphene is atomically thin, a 2D treatment is sufficient. With the in-plane lattice constant a the primitive reciprocal lattice vectors can be taken as

$$\vec{a}^* = \frac{2\pi}{a} \begin{pmatrix} 1/\sqrt{3} \\ 1 \end{pmatrix}, \quad \vec{b}^* = \frac{2\pi}{a} \begin{pmatrix} 1/\sqrt{3} \\ -1 \end{pmatrix}. \quad (\text{A.6})$$

The simplest pseudopotential calculation that yields the threefold symmetry around the K [$\vec{K} = (2\vec{a}^* + \vec{b}^*)/3$] point needs three reciprocal lattice vectors, namely $\vec{g}_1 = 0$, $\vec{g}_2 = \vec{a}^*$ and $\vec{g}_3 = \vec{a}^* + \vec{b}^*$, which are on an equilateral triangle with K in the centre. For this calculation the three possible Fourier components of the potential have the same value because of lattice symmetry. This value is determined so that the band structure calculation yields the same energy for the lower band at the Γ point as the experiment [37]. In this band structure calculation the Fermi velocity v_F is nearly independent of the form factor. It is determined essentially by the free-electron mass m_0 and graphene's lattice constant a , $v_F = h/(3m_0a) = 10^6 \text{ m s}^{-1}$. The results shown in figure 4 were obtained from a calculation using 21 reciprocal lattice vectors, also oriented symmetrically around the K point.

One advantage of this calculation is that it is very easy to incorporate the matter–light coupling by replacing $\hbar\vec{k}$ in (A.5) with $\hbar\vec{k} + e\vec{A}(t)$ (see section 4).

References

- [1] Castro Neto A H, Guinea F, Peres N M R, Novoselov K S and Geim A K 2009 The electronic properties of graphene *Rev. Mod. Phys.* **81** 109
- [2] Nair R R, Blake P, Grigorenko A N, Novoselov K S, Booth T J, Stauber T, Peres N M R and Geim A K 2008 Fine structure constant defines visual transparency of graphene *Science* **320** 1308

- [3] Mak K F, Sfeir M Y, Wu Y, Lui C H, Misewich J A and Heinz T F 2008 Measurement of the optical conductivity of graphene *Phys. Rev. Lett.* **101** 196405
- [4] Wegener M 2005 *Extreme Nonlinear Optics* (Berlin: Springer)
- [5] Strait J H, Wang H, Shivaraman S, Shields V, Spencer M and Rana F 2011 Very slow cooling dynamics of photoexcited carriers in graphene observed by optical-pump terahertz-probe spectroscopy *Nano Lett.* **11** 4902
- [6] Frenzel A J, Lui C H, Fang W, Nair N L, Herring P K, Jarillo-Herrero P, Kong J and Gedik N 2013 Observation of suppressed terahertz absorption in photoexcited graphene *Appl. Phys. Lett.* **102** 113111
- [7] Jnawali G, Rao Y, Yan H and Heinz T F 2013 Observation of a transient decrease in terahertz conductivity of single-layer graphene induced by ultrafast optical excitation *Nano Lett.* **13** 524
- [8] Winnerl S *et al* 2011 Carrier relaxation in epitaxial graphene photoexcited near the Dirac point *Phys. Rev. Lett.* **107** 237401
- [9] Woerner M, Kuehn W, Bowlan P, Reimann K and Elsaesser T 2013 Ultrafast two-dimensional terahertz spectroscopy of elementary excitations in solids *New J. Phys.* **15** 025039
- [10] Paul M J, Chang Y C, Thompson Z J, Stickel A, Wardini J, Choi H, Minot E D, Norris T B and Lee Y S 2013 High-field terahertz response of graphene *New J. Phys.* **15** 085019
- [11] Hwang H Y, Brandt N C, Farhat H, Hsu A L, Kong J and Nelson K A 2013 Nonlinear THz conductivity dynamics in *p*-type CVD-grown graphene *J. Phys. Chem. B* **117** 15819–24
- [12] Kuehn W, Reimann K, Woerner M and Elsaesser T 2009 Phase-resolved two-dimensional spectroscopy based on collinear *n*-wave mixing in the ultrafast time domain *J. Chem. Phys.* **130** 164503
- [13] Kuehn W, Reimann K, Woerner M, Elsaesser T and Hey R 2011 Two-dimensional terahertz correlation spectra of electronic excitations in semiconductor quantum wells *J. Phys. Chem. B* **115** 5448
- [14] Reimann K 2007 table-top sources of ultrashort THz pulses *Rep. Prog. Phys.* **70** 1597
- [15] Wu Q and Zhang X C 1995 Free-space electro-optic sampling of terahertz beams *Appl. Phys. Lett.* **67** 3523
- [16] Stroucken T, Knorr A, Thomas P and Koch S W 1996 Coherent dynamics of radiatively coupled quantum-well excitons *Phys. Rev. B* **53** 2026
- [17] Sprinkle M *et al* 2009 First direct observation of a nearly ideal graphene band structure *Phys. Rev. Lett.* **103** 226803
- [18] Spitzer W G, Kleinman D and Walsh D 1959 Infrared properties of hexagonal silicon carbide *Phys. Rev.* **113** 127
- [19] Breusing M, Kuehn S, Winzer T, Malić E, Milde F, Severin N, Rabe J P, Ropers C, Knorr A and Elsaesser T 2011 Ultrafast nonequilibrium carrier dynamics in a single graphene layer *Phys. Rev. B* **83** 153410
- [20] Song J C W, Reizer M Y and Levitov L S 2012 Disorder-assisted electron-phonon scattering and cooling pathways in graphene *Phys. Rev. Lett.* **109** 106602
- [21] Malić E, Winzer T, Bobkin E and Knorr A 2011 Microscopic theory of absorption and ultrafast many-particle kinetics in graphene *Phys. Rev. B* **84** 205406
- [22] Grönqvist J H, Stroucken T, Lindberg M and Koch S W 2012 Wannier excitons signalling strong Coulomb coupling in graphene *Eur. Phys. J. B* **85** 395
- [23] Ishikawa K L 2010 Nonlinear optical response of graphene in time domain *Phys. Rev. B* **82** 201402
- [24] Ishikawa K L 2013 Electronic response of graphene to an ultrashort intense terahertz radiation pulse *New J. Phys.* **15** 055021
- [25] Cohen M L and Bergstresser T K 1966 Band structures and pseudopotential form factors for fourteen semiconductors of the diamond and zinc-blende structures *Phys. Rev.* **141** 789
- [26] van Haeringen W and Junginger H G 1969 Pseudopotential approach to the energy band structure of graphite *Solid State Commun.* **7** 1723
- [27] Mohan B, Kumar A and Ahluwalia P K 2012 A first principle study of interband transitions and electron energy loss in mono and bilayer graphene: effect of external electric field *Physica E* **44** 1670
- [28] Dawlaty J M, Shivaraman S, Strait J, George P, Chandrashekhara M, Rana F, Spencer M G, Veksler D and Chen Y 2008 Measurement of the optical absorption spectra of epitaxial graphene from terahertz to visible *Appl. Phys. Lett.* **93** 131905

- [29] Schlicher R R, Becker W, Bergou J and Scully M O 1984 Interaction Hamiltonian in quantum optics or: $\vec{p} \cdot \vec{A}$ versus $\vec{E} \cdot \vec{r}$ revisited *Proc. NATO ASI on Quantum Electrodynamics and Quantum Optics (Boulder, CO, 1983)* ed A O Barut (New York: Plenum) pp 405–41
- [30] Kuehn W, Gaal P, Reimann K, Woerner M, Elsaesser T and Hey R 2010 Coherent ballistic motion of electrons in a periodic potential *Phys. Rev. Lett.* **104** 146602
- [31] Mikhailov S A and Ziegler K 2007 New electromagnetic mode in graphene *Phys. Rev. Lett.* **99** 016803
- [32] Stauber T, Peres N M R and Geim A K 2008 Optical conductivity of graphene in the visible region of the spectrum *Phys. Rev. B* **78** 085432
- [33] Choi H, Borondics F, Siegel D A, Zhou S Y, Martin M C, Lanzara A and Kaindl R A 2009 Broadband electromagnetic response and ultrafast dynamics of few-layer epitaxial graphene *Appl. Phys. Lett.* **94** 172102
- [34] Yan H, Xia F, Zhu W, Freitag M, Dimitrakopoulos C, Bol A A, Tulevski G and Avouris P 2011 Infrared spectroscopy of wafer-scale graphene *ACS Nano* **5** 9854
- [35] Horn J *et al* 2011 Drude conductivity of Dirac fermions in graphene *Phys. Rev. B* **83** 165113
- [36] Bloch F 1929 Über die Quantenmechanik der Elektronen in Kristallgittern *Z. Phys.* **52** 555
- [37] Kralj M, Pletikoscic I, Petrovic M, Pervan P, Milun M, N'Diaye A T, Busse C, Michely T, Fujii J and Vobornik I 2011 Graphene on Ir(111) characterized by angle-resolved photoemission *Phys. Rev. B* **84** 075427